

## Article

# C<sub>2</sub>O Nanotubes with Negative Strain Energies and Improvements of Thermoelectric Properties via N-Doping Predicted from First-Principle Calculations

Jianbao Wu \* , Liyuan Jiang, Xiaoyi Li and Zhixiang Yin

School of Mathematics, Physics and Statistics, Shanghai University of Engineering Science, 333 Longtong Road, Shanghai 201620, China

\* Correspondence: wujianbao@sues.edu.cn

**Abstract:** In this study, the geometric structure, strain energy, and electronic properties of armchair C<sub>2</sub>O nanotubes (A-C<sub>2</sub>ONTs(n, n)) and zigzag C<sub>2</sub>O nanotubes (Z-C<sub>2</sub>ONTs(n, 0)) are studied in detail. The results show that these nanotubes behave as special shapes; the section of Z-C<sub>2</sub>ONTs(n, 0) along the axial direction is an n-edge type, and the section tends to be round with an increase in n while the boundary of section along the axial direction for A-C<sub>2</sub>ONTs(n, n) fluctuates. With an increase in n, the fluctuation disappears gradually, and the section also tends to be round. Compared with C<sub>2</sub>O nanosheets (g-C<sub>2</sub>O), C<sub>2</sub>O nanotubes have similar or even smaller strain energy, when the tube diameter is greater than or equal to 15 Å, the strain energy begins to show a negative value, and the negative value tends to be stable as the pipe diameter increases. Z-C<sub>2</sub>ONTs start to show negative strain energies from n = 8 and A-C<sub>2</sub>ONTs from n = 12, indicating their higher stabilities relative to the g-C<sub>2</sub>O sheets. The calculation of the electronic band structure shows that Z-C<sub>2</sub>ONTs are an indirect band gap semiconductor, and A-C<sub>2</sub>ONT is a direct band gap semiconductor. The band gap value of Z-C<sub>2</sub>ONTs first increases and then stabilizes with the diameters of the nanotubes, and the band gap value of A-C<sub>2</sub>ONTs decreases with the increase in the nanotubes and tends to the band gap value of the g-C<sub>2</sub>O sheet. In addition, the electronic properties and thermoelectric properties of C<sub>2</sub>ONTs(n = 4, 6, 8) before and after N-doping were also studied. We found that N-doping changed the electronic and thermoelectric properties of C<sub>2</sub>ONTs. It reduced the nanotube band gap value and significantly improved the thermoelectric figures of merit of Z-C<sub>2</sub>ONTs(n = 4, 6, 8) and A-C<sub>2</sub>ONT(4, 4), which comprised an effective strategy to improve the thermoelectric figure of merit of nanotubes. The results showed that the C<sub>2</sub>ONTs had potential as thermoelectric materials after N-doping, which provided important guidance for designing low-dimensional g-C<sub>2</sub>O nanostructures.

**Keywords:** density functional theory; C<sub>2</sub>ONTs; negative strain energy; thermoelectric figure of merit



**Citation:** Wu, J.; Jiang, L.; Li, X.; Yin, Z. C<sub>2</sub>O Nanotubes with Negative Strain Energies and Improvements of Thermoelectric Properties via N-Doping Predicted from First-Principle Calculations. *Crystals* **2023**, *13*, 1097. <https://doi.org/10.3390/cryst13071097>

Academic Editors: Małgorzata Hołyńska and Ionut Tranca

Received: 13 June 2023

Revised: 9 July 2023

Accepted: 10 July 2023

Published: 13 July 2023



**Copyright:** © 2023 by the authors. Licensee MDPI, Basel, Switzerland. This article is an open access article distributed under the terms and conditions of the Creative Commons Attribution (CC BY) license (<https://creativecommons.org/licenses/by/4.0/>).

## 1. Introduction

Graphene is an ideal choice for next-generation devices due to its excellent physical and chemical properties [1–4]. However, one of the main obstacles is the zero-band gap of graphene, which has limited its applications in some fields. Therefore, there have been many studies on adjusting the band gap of graphene. Among them, atom doping is a typical method, such as in C<sub>2</sub>N [5,6], C<sub>3</sub>N [7,8], and C<sub>3</sub>N<sub>4</sub> [9,10] nanosheets formed by nitrogen (N) doping, which not only opens the band gap but also provides a stable structure and good performance. Furthermore, these carbon–nitrogen nanomaterials have been synthesized experimentally [11,12]. Nonetheless, when synthesizing these N-rich carbon nitride materials, the easy releases and stabilities of N<sub>2</sub> molecules become its disadvantages [13]. In the past decades, a number of researchers have reported that oxygen doping can also adjust the band gap of graphene [14–16] and provides a more stable structure and performance [17,18]. As a case study, Liu et al. [19] theoretically proposed the insertion of 18-crown-6 ether embedded into graphene with  $2\sqrt{3} \times 2\sqrt{3}$  units to obtain

a single layer of graphitized carbon with an O pore structure, named as graphitized carbon oxide ( $g\_C_2O$ ), which has a wide band gap and good superconductivity, thermal stability, and the function of screening gases [20,21]. In addition, its structure and performance are similar to Graphene [22],  $C_3N_4$  [23], and  $C_2N$  [6,24]. The excellent properties of these materials make them the hope of the next generation of nano-electronic devices.

One-dimensional nanotubes can be obtained by curling two-dimensional nanosheets in a specific direction. Research on nanotubes in low-dimensional materials is also very extensive. For nanotubes, it can also be used in high-capacity batteries [25,26], gas sensors [27–29], thermoelectric materials [30], and so on. Among them, research on carbon nanotubes is the earliest and most comprehensive. Studies over the past decades have provided important information on new-type inorganic nanotubes. These have shown that only a small percentage of nanotubes have negative strain energies, which can provide bases for experimental synthesis. For example, the strain energy of  $Ti_2CO_2$  nanotubes (16, 16) is  $-0.18$  eV [31], the strain energy of InSb nanotubes (6, 6) is  $-0.17$  eV [32], and the strain energy of stanene-based nanotubes (5, 0) is  $-0.05$  eV [33,34], indicating that they are easily rolled from two-dimensional nanosheets. From the literature reports so far, there have been many studies on the nanotubes formed by nanosheets, which not only have lower energies and superior band gaps but also have more novel properties than nanosheets [18,35]. According to recently literature, research into  $g\_C_2O$  nanotubes has been a largely under-explored domain, too little work has been devoted to them.

In recent years, due to global industrialization, the waste of energy has become more and more serious, which has affected the economic development and national life of some countries and regions. Researchers' interest in thermoelectric materials has increased dramatically [36–39], and finding or improving the thermoelectric properties of materials is a hot topic of current research. The efficiency of thermoelectric performance is judged based on the size of the thermoelectric figure of merit ( $ZT$ ). The  $ZT$  is mainly calculated by the equation  $ZT = S^2\sigma T / K$ , where  $T$  is the temperature,  $S^2\sigma$  is the power factor,  $S$  is the Seebeck coefficient,  $K$  ( $K = K_e + K_{ph}$ ) is the thermal conductivity,  $K_e$  is the electronic thermal conductivity, and  $K_{ph}$  is the phonon thermal conductivity. It can be seen from the formula that the smaller thermal conductivity and the larger power factor are the reasons for a larger  $ZT$  value. However, traditional thermoelectric materials with large  $ZT$  values often include heavy metals such as Bi and Te [40,41]; these elements are generally expensive or toxic. In contrast, carbon-based materials are environmentally friendly and widely distributed in the universe. The use of low-dimensional carbon nanomaterials as thermoelectric materials can improve this shortcoming. However, both carbon nanotubes ( $K > 1000$  W/m·K) and graphene ( $K \sim 3500$ – $5300$  W/m·K) have higher thermal conductivities [36,42], which are also their frequently stated problems as thermoelectric materials. In order to reduce the high thermal conductivity of low-dimensional carbon nanomaterials, Avery et al. [42] combined theoretical and experimental studies show that doped networks in SWCNTs could greatly reduce thermal conductivities and improve thermoelectric performances. On the other hand, based on experiments, Liam and Joseph [43] found that n-type doping of SWCNT could effectively improve the thermoelectric efficiencies of carbon nanotubes. At the same time, theoretical studies have found that N-doped graphene could also significantly reduce the thermal conductivity of graphene. The lattice thermal conductivity of  $C_2N$  decreases by two orders of magnitude, which are around  $40$  W/m·K at  $300$  K along both the zigzag and armchair directions [44]. Moreover, by comparing the thermal conductivities of  $C_3N$  nanotubes with carbon nanotubes of the same tube diameter and length, it was found that the thermal conductivities of  $C_3N$  nanotubes were significantly lower than those of carbon nanotubes [45,46], such as at  $600$  nm. The conductivity of (5, 5)  $C_3NNT$  was  $519.8$  W/m·K which was considerably lower than the conductivity of the (10, 10) CNT, which was  $1242.6$  W/m·K.

Up to now, as far as we know, there is no research on the structures and performances of  $C_2O$  nanotubes ( $C_2ONTs$ ). In order to understand the electronic structures, stabilities, and thermoelectric properties of  $C_2ONTs$ , in this work, nanotubes formed from  $g\_C_2O$

sheets were studied based on density functional theory. The considered nanotubes included two types of structure, armchair and zigzag, with diameters between 3.78–40.75 Å and 2.69–23.59 Å, respectively. The optimal geometries, strain energies, and electronic properties of the nanotubes were considered, and the calculation results showed that  $Z\_C_2ONTs(n, 0)$  started to show negative strain energies from  $n = 8$  and  $A\_C_2ONTs(n, n)$  from  $n = 12$  when being compared with  $C_2O$  nanosheets ( $g\_C_2O$ ). In view of that, many researchers have performed more research on the thermoelectric properties of carbon nanotubes [37,42], and N-doping could also improve the thermoelectric properties of graphene [46]. Here, we have calculated the thermoelectric properties before and after  $C_2ONTs$  were doped with N, which included the three armchair types (4, 4), (6, 6), and (8, 8) and the three zigzag types (4, 0), (6, 0), and (8, 0). Through calculation and analysis of Seebeck's coefficient (S) and thermal conductivity (K), the results showed that  $A\_C_2ONTs$  could greatly increase the ZT value in the temperature range of (200, 800) through N-doping, whereas the impact of N-doping on  $Z\_C_2ONTs$  was not evident.

## 2. Computational Details

The calculated  $C_2ONT$  could be formed by curling  $g\_C_2O$  nanosheets; thus, the chiral vector of carbon nanotubes  $C_h = ma_1 + na_2$  [47] was used to represent, and the  $a_1$  and  $a_2$  chiral vectors were unit carriers of  $g\_C_2O$  nanosheets (Figure 1) and zigzag nanotubes ( $Z\_C_2ONT$ ) when  $z = 0$  and armchair nanotubes ( $A\_C_2ONT$ ) when  $n = m$ . In this study,  $Z\_C_2ONT(n, 0)$  and  $A\_C_2ONT(n, n)$  were constructed using Material Studio (where  $n = 2, 4, 6, 8, 10, 12, 14, 16, 18$ ). For the two different types of nanotubes considered in this paper, the supercell contained 36–324 atoms (listed in Table S1), and all calculations were performed in the VASP (Vienna Ab Simulation Package) software [48,49]. The Device Studio [50] program provided a number of functions of performing visualization, modeling, and simulation. The exchange correlation function used the generalized gradient approximation GGA method [51], parameterized by Pedrew–Burke–Ernzerh (PBE), with plane waves up to a cutoff energy of 500 eV. Brillouin zone integration was performed using a  $1 \times 1 \times 12$  k-point grid. All geometric structures were fully relaxed and optimized until the force on the atoms was less than  $0.02 \text{ eV \AA}^{-1}$ , and the convergence criterion for electron self-consistency was set to  $10^{-5} \text{ eV}$ . In order to avoid possible coupling between the atoms, the vacuum area between the nanotubes was set to  $20 \text{ \AA}$  so that the interactions between the nanotubes were negligible. In order to obtain an optimized structure, we considered the  $C_2ONT$  unit to relax in the axial direction until the stress component was less than 0.1 GPa. The phonon spectra of force constants were calculated using PHONOPY code, based on the VASP-DFPT [52] (density functional perturbation theory) interface, using a  $1 \times 1 \times 5$  supercell with the k-points set to  $1 \times 1 \times 7$ . Born–Oppenheimer ab initio molecular dynamics (AIMD) simulations were employed to evaluate the stability of  $C_2ONT$ . In total,  $1 \times 1 \times 5$  supercells of  $Z\_C_2ONT(8, 0)$  and  $A\_C_2ONT(12, 12)$  containing 144 and 216 atoms, respectively, were used to reduce the lattice translation constraints. In this case, the system was stable for 10 ps at 300 K with a time step of 1 fs, in addition to its temperature control with the Nosé algorithm [53]. Finally, we also calculated the thermoelectric performances of the  $C_2O$  nanotubes. To confirm the accuracy of the thermal property's calculation, we first calculated the ZT values of SWCNT (7, 0) and (10, 0), which are shown in Figure S1 (in Supplementary Materials). According to the calculated results, the ZT values of (7, 0) and (10, 0) at 300 K were 0.14 and 0.19, which were consistent with those calculated by Jiang et al. [54]. All the thermal property calculations were performed by Quantum ESPRESSO [55].

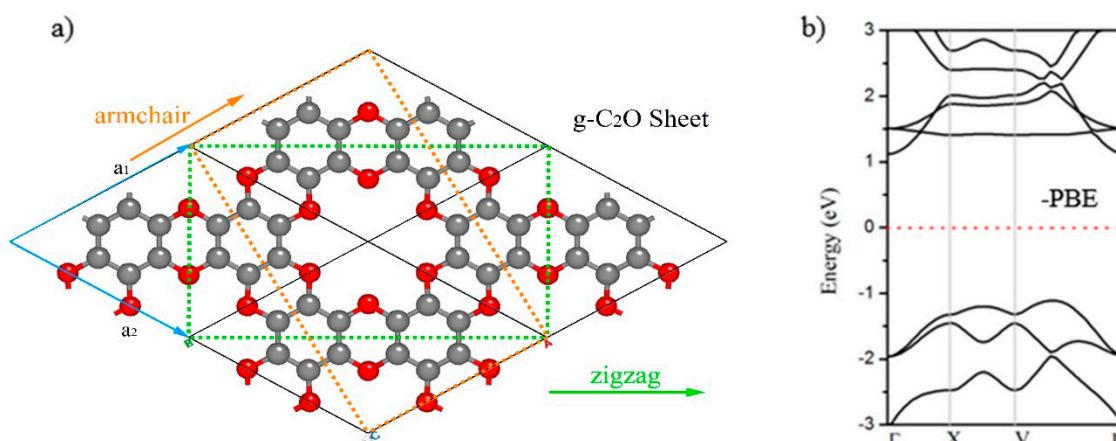


**Figure 1.** (a) Schematic of rolling g-C<sub>2</sub>O nanosheet to zigzag and armchair nanotube structures; (b) Electronic band structure of g-C<sub>2</sub>O nanosheet.

### 3. Results and Discussion

#### 3.1. Electronic Properties

The first issue discussed is the g-C<sub>2</sub>O nanosheet. After being fully optimized, the single-layer g-C<sub>2</sub>O nanosheet behaves with C-C and C-O bond lengths of 1.38 Å and 1.39 Å, C-O-C and O-C-C bond angles of 115.72° and 117.86°, and a pore size of 5.37 Å. The electronic band structure g-C<sub>2</sub>O nanosheet also has been calculated and plotted in Figure 1b. As shown in Figure 1b, the g-C<sub>2</sub>O is a semiconductor with an indirect band gap of 2.27 eV, which is in good agreement with the theoretical studies [17,19]. Therefore, it can be seen from Figure 1a that the single-layer g-C<sub>2</sub>O nanosheets are rolled along specific two directions (as shown in Figure 1a); thus, the Z-C<sub>2</sub>ONT(*n*, 0) and A-C<sub>2</sub>ONT(*n*, *n*) can be formed from g-C<sub>2</sub>O nanosheets theoretically.

The second issue discussed comprised the C<sub>2</sub>ONTs, the bond length, and bond angle of the fully optimized Z-C<sub>2</sub>ONT(*n*, 0) and A-C<sub>2</sub>ONT(*n*, *n*), given in Table S1. With the increase in *n* of the C<sub>2</sub>ONTs, both the bond length and bond angle of the two types of C<sub>2</sub>ONTs decreased and closed to that of g-C<sub>2</sub>O nanosheet. The changes in bond length and bond angle reflected the structural stability of the C<sub>2</sub>ONTs, which could be confirmed by the calculation of the strain energies of C<sub>2</sub>ONTs. The optimized structural shapes of the C<sub>2</sub>ONTs are shown in Figure 2. We can see from Figure 2 that the structural shapes of Z-C<sub>2</sub>ONTs are different from those of A-C<sub>2</sub>ONTs. As for Z-C<sub>2</sub>ONTs, when *n* = 2, the structure appeared as a hollow elliptical cylinder after full optimization; when *n* = 4, it appeared as a hollow quadrangular prism; as shown in Figure S2, when *n* = 6, it became a hollow hexagonal prism; when *n* = 8, it became a hollow octagonal prism; and, according to the above rules, hollow prisms began to tend to become hollow cylinders as the tube size increased. Optimized A-C<sub>2</sub>ONTs appeared as a square cylinder structure when *n* = 2 and started to become an empty cylindrical structure after *n* = 4, but the cylindrical surface undulated; as shown in Figures S3 and S4, it started to appear as an empty cylindrical structure with smooth surface fluctuations when *n* = 12, and A-C<sub>2</sub>ONT was an empty cylindrical structure with almost no undulations on the surface when *n* = 18. This was mainly because the number of atoms in the system increased, the bending effects of the nanotubes became smaller and smaller, the structures gradually stabilized [32], the intermolecular forces became smaller, the bond lengths and bond angles were stable, and the structures tended to be gradually stable. The unique nanotube structure of C<sub>2</sub>ONT was slightly similar to the structure of a g-C<sub>3</sub>N<sub>4</sub> nanotube [18].

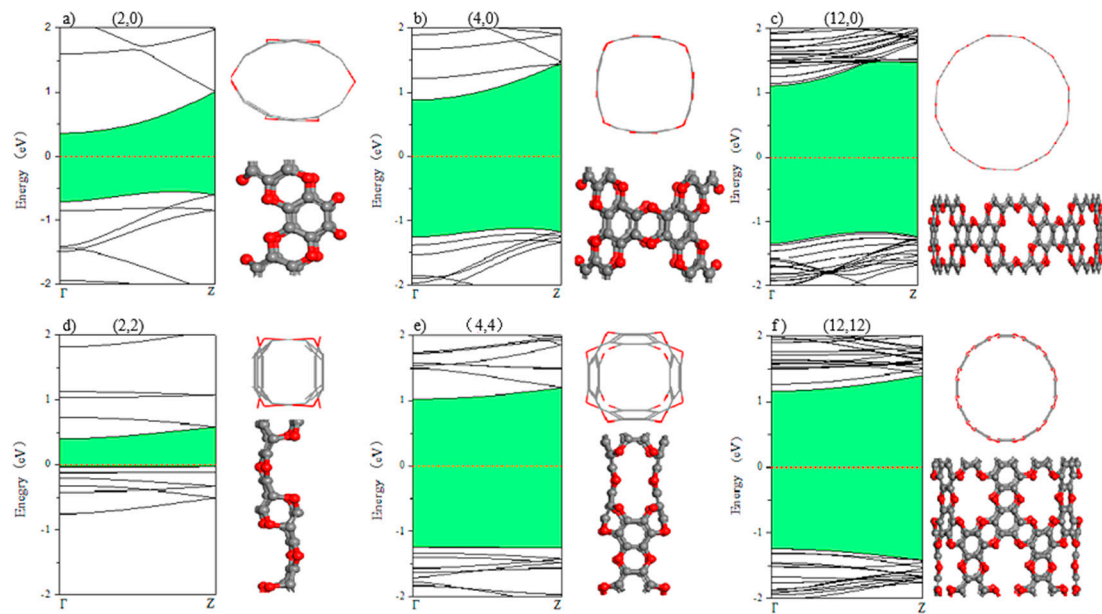


**Figure 2.** The band structure of Z\_C<sub>2</sub>ONT and A\_C<sub>2</sub>ONT on the left, the top view of the linear structure, and the side view of the club structure on the right: (a)(2,0); (b)(4,0); (c)(12,0); (d)(2,2); (e)(4,4); (f)(12,12).

Strain energy  $E_{str}$  is a measure of the stability and feasibility of nanotubes compared to single-layer structures [33]. In order to evaluate the stability of C<sub>2</sub>ONT, we calculated its strain energy ( $E_{str}$ ), which is defined as  $E_{str} = (E_{Nanotube} - E_{Nanosheet}) / unitcell$ , where  $E_{Nanotube}$  and  $E_{Nanosheet}$  refer to the energies of the C<sub>2</sub>ONT and g\_C<sub>2</sub>O nanosheets with the same number of primary unit cells, respectively (each primary unit cell contains two C and one O atoms). The corresponding strain energy values of Z\_C<sub>2</sub>ONT and A\_C<sub>2</sub>ONT are shown in Table 1.

**Table 1.** Strain energy values, tube diameters, and band gap ( $E_{gap}$ ) values of C<sub>2</sub>ONT.

	g-C <sub>2</sub> O	$E_{str}$ (meV/Unit Cell)	Diameter (Å)	$E_{gap}$
<b>Nanosheet</b>	(0, 0)	-	-	2.27 <sup>i</sup>
	(2, 0)	533.0	3.78	1.07 <sup>i</sup>
	(4, 0)	75.3	8.55	2.14 <sup>i</sup>
	(6, 0)	9.9	13.24	2.35 <sup>i</sup>
	(8, 0)	−8.9	17.80	2.46 <sup>i</sup>
	(10, 0)	−17.5	22.45	2.47 <sup>i</sup>
	(12, 0)	−22.2	27.08	2.45 <sup>i</sup>
	(14, 0)	−25.0	31.62	2.45 <sup>i</sup>
	(16, 0)	−26.2	36.21	2.44 <sup>i</sup>
<b>Zigzag (n, 0)</b>	(18, 0)	−27.9	40.75	2.44 <sup>i</sup>
	(2, 2)	1911.8	2.69	0.41 <sup>d</sup>
	(4, 4)	351.1	4.96	2.25 <sup>d</sup>
	(6, 6)	115.6	7.80	2.27 <sup>d</sup>
	(8, 8)	34.0	10.45	2.58 <sup>d</sup>
	(10, 10)	6.1	13.06	2.53 <sup>d</sup>
	(12, 12)	−5.6	15.71	2.48 <sup>d</sup>
	(14, 14)	−14.0	18.36	2.41 <sup>d</sup>
	(16, 16)	−18.9	21.04	2.35 <sup>d</sup>
<b>Armchair (n, n)</b>	(18, 18)	−22.1	23.59	2.34 <sup>d</sup>

<sup>i</sup> means indirect gap and <sup>d</sup> means direct gap.

The relationship between strain energy and tube diameter or size parameter ( $n$ ) is shown in Figure 3. With the increase in diameter or parameter ( $n$ ), the strain energy values of Z-C<sub>2</sub>ONTs and A-C<sub>2</sub>ONTs all decreased. As seen from Figure 3b, when the tube diameter was greater than or equal to 15 Å, the strain energy began to show a negative value, and the negative value tended to be stable as the tube diameter increased. As seen from Figure 3a, when  $n = 8$  for Z-C<sub>2</sub>ONT and  $n = 12$  for A-C<sub>2</sub>ONT, the strain energy started to be negative. Negative strain energy meant that these C<sub>2</sub>ONTs had strong mechanical stabilities. To further study their thermal stabilities, the phonon spectra of Z-C<sub>2</sub>ONT ( $n, 0$ ) and A-C<sub>2</sub>ONT ( $n, n$ ) were calculated and are shown in Figure 4. From the phonon spectrum in Figure 4, it can be seen that there was no virtual frequency observed when the diameter of the tube changed from 4 Å to 18 Å, indicating that the nanotube structure was stable from the perspective of vibration spectrum; as the pipe diameter increased, there was a significant separation between the high-frequency and low-frequency parts. On the other hand, AIMD simulation at 300 K was further investigated the stability of C<sub>2</sub>ONT, which is shown in Figure S5. Within 1 ns, there was no significant deformation observed in the dynamic simulations of A-C<sub>2</sub>ONT (8, 0) and Z-C<sub>2</sub>ONT (12, 12), indicating good thermal stabilities. These stabilities were due to the orbital overlaps between adjacent atoms caused by the small diameter of C<sub>2</sub>ONT, but the adjacent orbital atoms no longer overlapped when the diameter was larger [33]. In the case of the same parameter  $n$ , the strain energy of Z-C<sub>2</sub>ONT was smaller than the corresponding A-C<sub>2</sub>ONT. Therefore, Z-C<sub>2</sub>ONT was more stable than the corresponding A-C<sub>2</sub>ONT. The reason was that the diameter of Z-C<sub>2</sub>ONT was larger than the diameter of A-C<sub>2</sub>ONT with the same value of  $n$ . From the definition formula of strain energy ( $E_{str}$ ), the smaller and smaller strain energy indicated that the energy required for various nanotubes formed by g-C<sub>2</sub>O nanosheets rolling up decreased with increasing tube diameter. This meant that the g-C<sub>2</sub>O nanosheets became easier to roll into nanotubes as the diameter increased. From another perspective, this was also expected because the g-C<sub>2</sub>O nanosheets with larger diameters had less deformations from the g-C<sub>2</sub>O nanosheets when rolled into nanotubes.

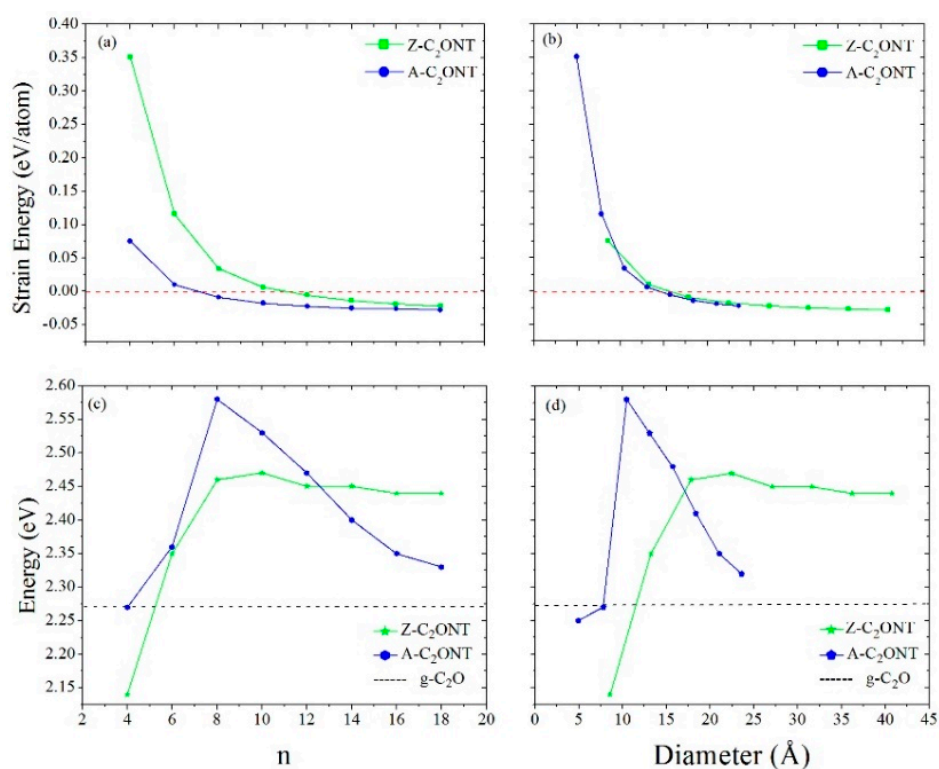


**Figure 3.** Strain energy as a function of (a) tube size  $n$ ; (b) diameter; (c) band gap as a function of tube size  $n$ ; and (d) diameter.

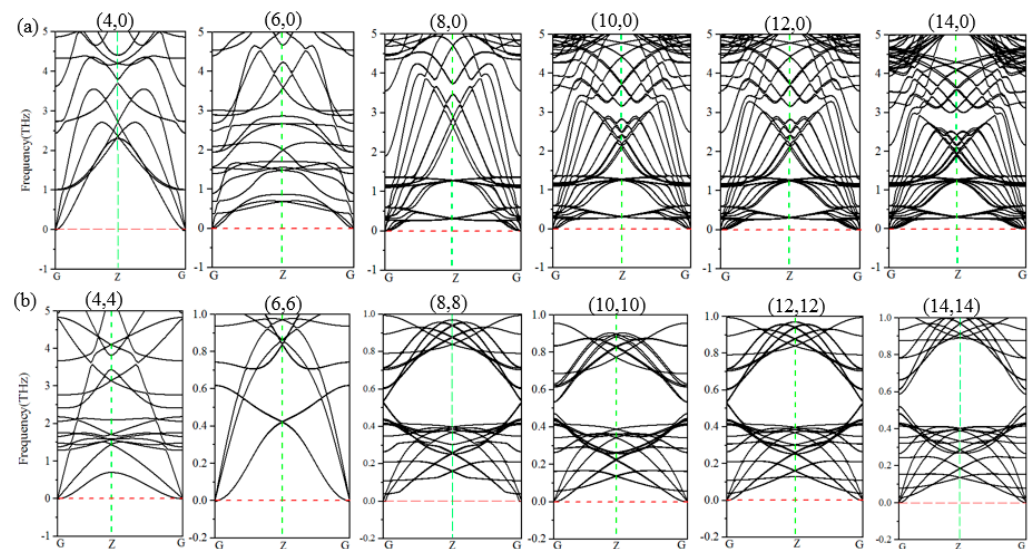


**Figure 4.** Phonon dispersion curves of  $C_2ONT$ , (a)  $Z\_C_2ONTs$ , and (b)  $A\_C_2ONTs$ , point Z line marked with green, and frequency of zero line marked with red.

We also calculated the electronic structures of  $Z\_C_2ONTs$  and  $A\_C_2ONTs$ . As can be seen from Table 1,  $Z\_C_2ONTs$  were all indirect band gap semiconductors, whereas  $A\_C_2ONTs$  were all direct band gap semiconductors. Figure 3c,d show the band gap as a function of the tube diameter and parameter ( $n$ ), respectively. It can be clearly seen from Figure 3 that the band gaps of  $C_2ONTs$  increased first with the increase in the diameter and  $n$ , and they then gradually approached convergence. It is worth mentioning that the band gaps of the  $A\_C_2ONTs$  converged to the value of the  $g\_C_2O$  nanosheet especially. As stated in the paragraph above, the degree of hybridization between the atomic orbitals changed with the bond length and band angle changes. As the tube diameter increased, the dependence of the band gap on the chirality and diameter became negligible, which was very similar to a  $C_2N$  nanotube [56].

### 3.2. Thermoelectric Properties

In order to investigate the thermoelectric performances of the  $C_2ONTs$ , we considered three cases for comparison when  $n = 4, 6, 8$  for  $A\_C_2ONTs(n, n)$  and  $Z\_C_2ONTs(n, 0)$ . While N-doping could improve the thermoelectric properties of graphene, the N-doped  $C_2ONTs$  ( $N\_C_2ONTs$ ) were also studied here. The method of doping was that the six oxygen atoms around the carbon ring were replaced by nitrogen. This doping was performed with reference to the structure of  $C_2N$  nanosheets. On the one hand,  $C_2N$  nanosheets have been successfully synthesized in the laboratory. On the other hand,  $C_2N$  nanotubes also have small strain energies. We calculated both the structure and ZT values of  $C_2NNT(4, 4)$  in Figure S8. After full optimization, the electronic structures of  $N\_C_2ONTs$  were calculated. The structures and electronic band structures of  $N\_C_2ONTs$  are shown in Figures S6 and S7. As seen from Figure S7, N-doping introduced impure energy bands between the band gaps but did not change the nature of the band gap; the zigzag type maintained the indirect band gap, whereas the armchair type kept the direct band gap unchanged. In terms of size, the band gap became smaller after N-doping.

First of all, the ZT values of the  $N\_C_2ONTs$  and  $C_2ONTs$  in the temperature range of (200 ~ 1000 K) were calculated separately. The curves of the ZT value changing with temperature of  $Z\_C_2ONTs$  before and after N-doping are shown in Figure 4a. In the temperature range of 200–400 K, the ZT value was almost zero. However, in the range of 400–800 K, the ZT value increased with the increase in temperature, and N-doping significantly increased the ZT value, especially for the (4, 0) tubes. Starting at 800 K, the ZT value of  $Z\_C_2ONTs$  after N-doping began to decrease with increasing temperature, whereas the undoped  $Z\_C_2ONTs$  still held the upward trend. For the  $A\_C_2ONTs$  case, as

shown in Figure 5b, the N-doping effect on the ZT value varied little, and the ZT value before and after N-doping was almost zero. The (4, 4) sample was an exception, as the ZT value after N-doping increased with temperature, reaching 0.17 at a temperature of 1000 K.

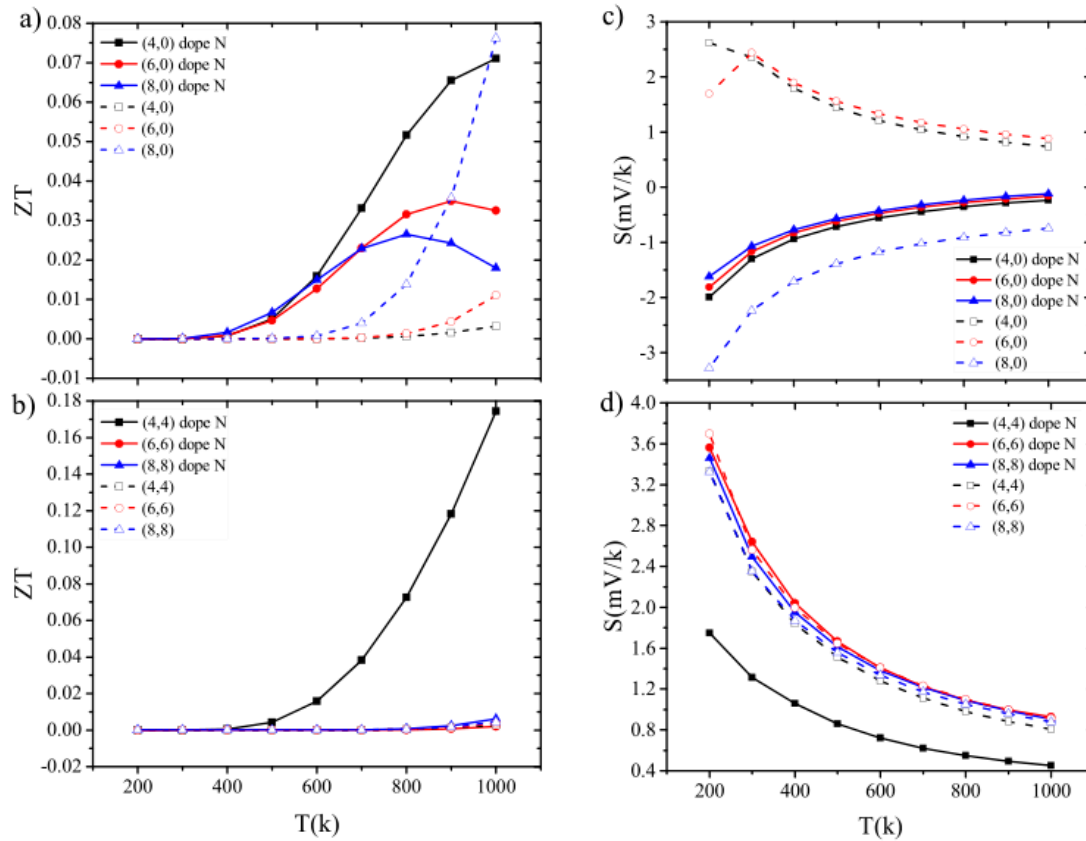


**Figure 5.** ZT value before and after N-doping as a function of temperature for (a) Z\_C<sub>2</sub>ONT and (b) A\_C<sub>2</sub>ONT. Seebeck coefficient before and after N-doping as a function of temperature for (c) Z\_C<sub>2</sub>ONT and (d) A\_C<sub>2</sub>ONT.

Figure 5c,d shows the Seebeck coefficients of the Z\_C<sub>2</sub>ONT and A\_C<sub>2</sub>ONT as a function of temperature. The N-doped Z\_C<sub>2</sub>ONT ( $n = 4, 6$ ) and A\_C<sub>2</sub>ONT ( $n = 4, 6, 8$ ) were both p-type semiconductors, and Z\_C<sub>2</sub>ONT (8,0) was an n-type semiconductor. It was noted that the Seebeck coefficients of the Z\_C<sub>2</sub>ONT and A\_C<sub>2</sub>ONT both decreased with increasing temperature. This was mainly because the number of electrons and holes of a non-degenerate semiconductor increased so that the carrier concentration would increase as the temperature increased, and the Seebeck coefficient was inversely proportional to the carrier concentration; therefore, the Seebeck coefficient decreased slightly. It could also be clearly seen from the figure that the Seebeck coefficient increased slightly as the tube size increased, but the overall value did not change much. Additionally, N-doped Z\_C<sub>2</sub>ONTs became n-type semiconductors, whereas A\_C<sub>2</sub>ONTs were P-type semiconductors, as before. As for the N-doped Z\_C<sub>2</sub>ONT, its Seebeck coefficient decreased with increasing temperature, as before. In contrast, the Seebeck coefficient of the N\_C<sub>2</sub>ONT decreased with increasing tube size, and the Seebeck coefficient was slightly smaller than that of the Z\_C<sub>2</sub>ONT. For the doped A\_C<sub>2</sub>ONT, the Seebeck coefficients of (6,6) and (8,8) had only small changes, whereas (4,4) had a significant decreasing trend, which was about twice, implying the independence of Seebeck coefficient with respect to the size of the armchair tube. As the Seebeck coefficient depended on the electronic structure near the Fermi level, it was related to the carrier concentration and the band shape. After the N-doped, the energy band gap was reduced, there was an evident impurity band near the Fermi level (as shown in Figure S7), and the intrinsic excitation of the N atom increased the carrier concentration

of the system and led to a decrease in the Seebeck coefficient. The Seebeck coefficient for the N-C<sub>2</sub>ONT(4, 4) nanotubes was significantly reduced, from a structural point of view, as the diameter of the (4, 4) nanotubes was 4.96 Å, which was much smaller than those of (6, 6) and (8, 8), which were 7.80 Å and 10.45 Å, respectively. Moreover, (4, 4) appeared as a hollow quadrangular prism, and the cylindrical surface undulated, as shown in Figure 2e. After N doping, the interaction between the N atoms and the C and O atoms was very strong, resulting in a rise in the concentrations of electrons or carriers in the system, which led to a significant drop in the Seebeck coefficient.

Thermal conductivity is another very important parameter that affects the thermoelectric performances of C<sub>2</sub>ONTs. The thermal conductivities of (4, 0), (6, 0), (8, 0), (4, 4), (6, 6), and (8, 8) have been calculated and shown in Figure 6c,d, respectively. The changing trend in the curve before and after N-doping is monotonous, and both increase with the increase in temperature. In addition, from Figure 6c,d, the influence of tube size is also the same.

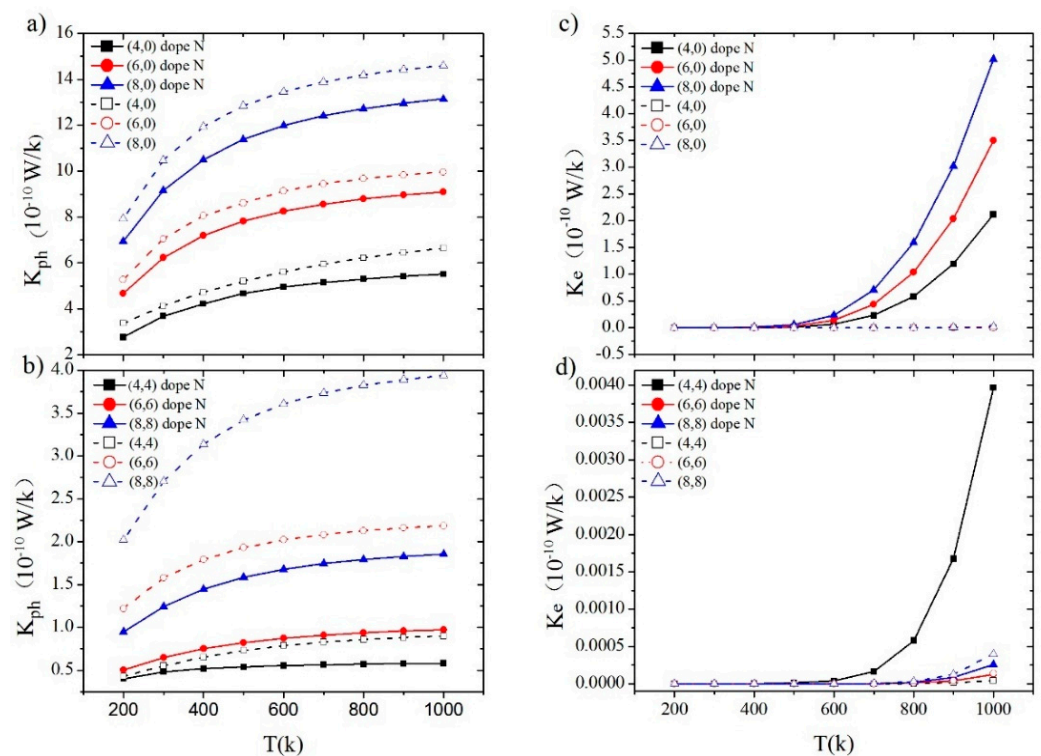


**Figure 6.** Phonon thermal conductance  $K_{ph}$  before and after N-doping as a function of temperature for (a) Z-C<sub>2</sub>ONTs and (b) A-C<sub>2</sub>ONTs. Electronic thermal conductivity  $K_e$  before and after N-doping as a function of temperature for (c) Z-C<sub>2</sub>ONTs and (d) A-C<sub>2</sub>ONTs.

Thermal conductivity includes electronic thermal conductivity  $K_e$  and phonon thermal conductivity  $K_{ph}$ .  $K_e$  and  $K_{ph}$  are also have been calculated and shown in Figure 6. As seen from Figure 6, with the temperature increasing, the  $K_{ph}$  values become bigger, and the N-doping makes the values of  $K_{ph}$  smaller, mainly because the introduction of impure atoms increases the scattering of phonons. However, the value of  $K_e$  is almost zero when less than 600 K, and the N-doping make the  $K_e$  values increase rapidly, especially for (4, 0), (6, 0), (8, 0), and (4, 4). Due to Wiedemann–Frenz’s law [57], the electronic thermal conductivity is proportional to the electrical conductivity of the material, and the electrical conductivity after N-doping increases; thus, their electronic thermal conductivity values  $K_e$  also increase. The decrease in phonon thermal conductivity caused by this N-doping is mainly due to the decrease in the average free path caused by the random disordered phonon scattering caused by the defect sites of N-doping.

#### 4. Conclusions

In this study, the geometric and electronic structures, parts of Z\_C<sub>2</sub>ONTs and A\_C<sub>2</sub>ONTs, were systematically studied using density functional theory. The results showed that Z\_C<sub>2</sub>ONTs and A\_C<sub>2</sub>ONT showed more peculiar configurations and had regularities in terms of structure. A comparison of the energies of the considered C<sub>2</sub>ONTs with the corresponding g\_C<sub>2</sub>O nanosheets showed that both the Z\_C<sub>2</sub>ONTs and A\_C<sub>2</sub>ONTs showed less strain energies. In particular, Z\_C<sub>2</sub>ONTs(n, 0) showed negative strain energy from n = 8 and A\_C<sub>2</sub>ONT(n, n) from n = 12, indicating that they were easier to synthesize. Electronic energy band calculations showed that both Z\_C<sub>2</sub>ONTs and A\_C<sub>2</sub>ONTs were semiconductors. Among them, Z\_C<sub>2</sub>ONT was an indirect band gap semiconductor, and A\_C<sub>2</sub>ONT was a direct band gap semiconductor. The band gap value of Z\_C<sub>2</sub>ONTs first increased and then stabilized with the diameter of the nanotubes. The band gap value of A\_C<sub>2</sub>ONTs decreased with the increase in the parameter n and tended to the band gap value of the g\_C<sub>2</sub>O nanosheet. Furthermore, the thermoelectric behaviors of the C<sub>2</sub>ONTs before and after N-doping were analyzed in detail. The calculation results showed that the band gap of the N-doped system was significantly reduced, and N-doping could significantly improve the thermoelectric figure of merit of the Z\_C<sub>2</sub>ONTs. In the original case, the Seebeck coefficient decreased with increasing temperature, and the power factor and thermal conductivity increased with increasing temperature and tube size. After N-doping, the characteristics of the entire system were affected. It reduced the Seebeck coefficient of the system; Z\_C<sub>2</sub>ONTs were all n-type semiconductors, and A\_C<sub>2</sub>ONTs were all p-type semiconductors. As the temperature increased, the power factors of some C<sub>2</sub>ONTs started to increase from lower temperatures. It also reduced the phonon thermal conductivities of all nanotubes. Although the electronic thermal conductivity of the system has improved, it only contributed to the thermal conductivity of a Z\_C<sub>2</sub>ONT at higher temperatures. The results showed that the C<sub>2</sub>ONTs had potential as thermoelectric materials after N-doping, which provided important guidance for designing low-dimensional g\_C<sub>2</sub>O nanostructures.

**Supplementary Materials:** The following supporting information can be downloaded at: <https://www.mdpi.com/article/10.3390/cryst13071097/s1>, Table S1: Optimized average bond length, average bond angle, and N\_atom (the number of atoms in unit cell) of g\_C<sub>2</sub>O nanosheets and C<sub>2</sub>O nanotubes. Figure S1: ZT value at 300 K for (a) SWCNT (7, 0) and (b) SWCNT (10, 0). Figure S2: The band structure of Z\_C<sub>2</sub>ONT and A\_C<sub>2</sub>ONT on the left, the top view of the linear structure, and the side view of the club structure on the right: (a) (6, 0); (b) (8, 0); (c) (6, 6); (d) (8, 8). Figure S3: The band structure of Z\_C<sub>2</sub>ONT and A\_C<sub>2</sub>ONT on the left, the top view of the linear structure, and the side view of the club structure on the right: (a) (10, 0); (b) (14, 0); (c) (10, 10); (d) (14, 14). Figure S4: The band structure of Z\_C<sub>2</sub>ONTs and A\_C<sub>2</sub>ONTs on the left, the top view of the linear structure, and the side view of the club structure on the right: (a) (16, 0); (b) (18, 0); (c) (16, 16); (d) (18, 18). Figure S5: The atomic structure of C<sub>2</sub>ONT in the AIMD simulation at 300 K after the time scale of 10 ps: (a) Z\_C<sub>2</sub>ONT (8, 0) and (b) A\_C<sub>2</sub>ONT (12, 12). Figure S6: The structure of C<sub>2</sub>ONT after N-doping. Figure S7: The band structure of C<sub>2</sub>ONT after N-doping. Figure S8: Trends in energy band structures, geometries, and ZT values of nanotubes with temperatures. (a) C<sub>2</sub>NNT (4, 4), (b) C<sub>2</sub>ONT (4, 4) doped with N, and (c) C<sub>2</sub>ONT (4, 4).

**Author Contributions:** Conceptualization, J.W. and Z.Y.; methodology, Z.Y.; software, L.J.; validation, X.L.; formal analysis, X.L.; investigation, L.J.; resources, X.L.; data curation, X.L.; writing—original draft preparation, X.L.; writing—review and editing, J.W.; visualization, L.J.; supervision, Z.Y.; project administration, Z.Y.; funding acquisition, Z.Y. All authors have read and agreed to the published version of the manuscript.

**Funding:** JBW was supported by the National Natural Science Foundation of China (No. 11047164), the Shanghai College Foundation for Excellent Young Teachers of China (No. gjd10023), and the Academic Program of Shanghai Municipal Education Commission (No. 11XK11 and 2011X34). ZXY was supported by the National Natural Science Foundation of China (No. 62072296).

**Institutional Review Board Statement:** Not applicable.

**Informed Consent Statement:** Not applicable.

**Data Availability Statement:** No new data were created or analyzed in this study. Data sharing is not applicable to this article.

**Acknowledgments:** JBW was supported by the National Natural Science Foundation of China (No. 11047164), the Shanghai College Foundation for Excellent Young Teachers of China (No. gjd10023), and the Academic Program of Shanghai Municipal Education Commission (No. 11XK11 and 2011X34). ZXY was supported by the National Natural Science Foundation of China (No. 62072296). We gratefully acknowledge HZWTECH for Kai Lin's help and discussions regarding this study.

**Conflicts of Interest:** The authors declare no conflict of interest.

## References

1. Zhou, X.; Zhao, C.H.; Wu, G.F.; Chen, J.H.; Li, Y.Q. DFT study on the electronic structure and optical properties of N, Al, and N-Al doped graphene. *Appl. Surf. Sci.* **2018**, *459*, 354–362. [[CrossRef](#)]
2. Feng, J.G.; Dong, H.Z.; Pang, B.L.; Shao, F.F.; Zhang, C.K.; Yu, L.Y.; Dong, L.F. Theoretical study on the optical and electronic properties of graphene quantum dots doped with heteroatoms. *Phys. Chem. Chem. Phys.* **2018**, *20*, 15244–15252. [[CrossRef](#)] [[PubMed](#)]
3. Avouris, P. Graphene: Electronic and Photonic Properties and Devices. *Nano Lett.* **2010**, *10*, 4285–4294. [[CrossRef](#)]
4. Alzebedeh, K.I. *Asme, Evaluation of Effective Elastic Mechanical Properties of Graphene Sheets*; Amer Soc Mechanical Engineers: New York, NY, USA, 2013; pp. 1205–1210.
5. Bafekry, A.; Stampfl, C.; Ghergherehchi, M.; Shayesteh, S.F. A first-principles study of the effects of atom impurities, defects, strain, electric field and layer thickness on the electronic and magnetic properties of the C<sub>2</sub>N nanosheet. *Carbon* **2020**, *157*, 371–384. [[CrossRef](#)]
6. Xu, B.; Xiang, H.; Wei, Q.; Liu, J.Q.; Xia, Y.D.; Yin, J.; Liu, Z.G. Two-dimensional graphene-like C<sub>2</sub>N: An experimentally available porous membrane for hydrogen purification. *Phys. Chem. Chem. Phys.* **2015**, *17*, 15115–15118. [[CrossRef](#)]
7. Bafekry, A.; Stampfl, C.; Shayesteh, S.F. A First-Principles Study of C<sub>3</sub>N Nanostructures: Control and Engineering of the Electronic and Magnetic Properties of Nanosheets, Tubes and Ribbons. *ChemPhysChem* **2020**, *12*, 164–174. [[CrossRef](#)]
8. Bafekry, A.; Shayesteh, S.F.; Peeters, F.M. C<sub>3</sub>N Monolayer: Exploring the Emerging of Novel Electronic and Magnetic Properties with Adatom Adsorption, Functionalizations, Electric Field, Charging, and Strain. *J. Phys. Chem. C* **2019**, *123*, 12485–12499. [[CrossRef](#)]
9. Yu, T.; Hu, Z.M.; Wang, H.M.; Tan, X. Enhanced visible-light-driven hydrogen evolution of ultrathin narrow-band-gap g-C<sub>3</sub>N<sub>4</sub> nanosheets. *J. Mater. Sci.* **2020**, *55*, 2118–2128. [[CrossRef](#)]
10. Liu, X.Q.; Kang, W.; Zeng, W.; Zhang, Y.X.; Qi, L.; Ling, F.L.; Fang, L.; Chen, Q.; Zhou, M. Structural, electronic and photocatalytic properties of g-C<sub>3</sub>N<sub>4</sub> with intrinsic defects: A first-principles hybrid functional investigation. *Appl. Surf. Sci.* **2020**, *499*, 6. [[CrossRef](#)]
11. Yang, S.W.; Li, W.; Ye, C.C.; Wang, G.; Tian, H.; Zhu, C.; He, P.; Ding, G.Q.; Xie, X.M.; Liu, Y.; et al. C<sub>3</sub>N-A 2D Crystalline, Hole-Free, Tunable-Narrow-Bandgap Semiconductor with Ferromagnetic Properties. *Adv. Mater.* **2017**, *29*, 7.
12. Luo, Z.Q.; Lim, S.H.; Tian, Z.Q.; Shang, J.Z.; Lai, L.F.; MacDonald, B.; Fu, C.; Shen, Z.X.; Yu, T.; Lin, J.Y. Pyridinic N doped graphene: Synthesis, electronic structure, and electrocatalytic property. *J. Mater. Chem.* **2011**, *21*, 8038–8044. [[CrossRef](#)]
13. Matar, S.F.; Wehrich, R. Strong p-magnetism in carbon suboxide C<sub>2</sub>O devised from first principles. *Chem. Phys. Lett.* **2017**, *674*, 115–119. [[CrossRef](#)]
14. Prias-Barragan, J.J.; Gross, K.; Ariza-Calderon, H.; Prieto, P. Graphene oxide multilayers: Synthesis, properties and possible applications in electronics. In Proceedings of the 2019 Latin American Electron Devices Conference (LAEDC), Armenia, Colombia, 24–27 February 2019; IEEE: New York, NY, USA, 2019; pp. 61–64.
15. Zhu, Y.W.; Murali, S.; Cai, W.W.; Li, X.S.; Suk, J.W.; Potts, J.R.; Ruoff, R.S. Graphene and Graphene Oxide: Synthesis, Properties, and Applications. *Adv. Mater.* **2010**, *22*, 3906–3924. [[CrossRef](#)] [[PubMed](#)]
16. Park, S.; Ruoff, R.S. Chemical methods for the production of graphenes. *Nat. Nanotechnol.* **2009**, *4*, 217–224, Erratum in *Nat. Nanotechnol.* **2010**, *5*, 309–309. [[CrossRef](#)]
17. Chen, Y.; Liu, G.H.; Li, Y.P.; Kong, L.J.; Liu, P.F. Structural Stability, Electronic and Magnetic Properties of O-doped Monolayer C<sub>2</sub>N. *Chin. J. Struct. Chem.* **2019**, *38*, 76–82.
18. Liu, J.J.; Cheng, B. New understanding of photocatalytic properties of zigzag and armchair g-C<sub>3</sub>N<sub>4</sub> nanotubes from electronic structures and carrier effective mass. *Appl. Surf. Sci.* **2018**, *430*, 348–354. [[CrossRef](#)]
19. Liu, W.; Liu, J.Y.; Miao, M.S. Macrocycles inserted in graphene: From coordination chemistry on graphene to graphitic carbon oxide. *Nanoscale* **2016**, *8*, 17976–17983. [[CrossRef](#)]
20. Qin, G.; Cui, Q.; Yun, B.; Sun, L.; Du, A.; Sun, Q. High capacity and reversible hydrogen storage on two dimensional C<sub>2</sub>N monolayer membrane. *Int. J. Hydrog. Energy* **2018**, *43*, 9895–9901. [[CrossRef](#)]
21. Liu, X.F.; Chang, X.; Zhu, L.; Li, X.F. High-efficiency helium separation through g-C<sub>2</sub>O membrane: A theoretical study. *Comput. Mater. Sci.* **2019**, *157*, 1–5. [[CrossRef](#)]
22. Nikkho, S.; Mirzaei, M.; Sabet, J.K.; Moosavian, M.A.; Hedayat, S.M. Enhanced quality of transfer-free graphene membrane for He/CH<sub>4</sub> separation. *Sep. Purif. Technol.* **2020**, *232*, 9. [[CrossRef](#)]

23. Guo, Y.; Tang, C.M.; Wang, X.B.; Wang, C.; Fu, L. Density functional calculations of efficient H<sub>2</sub> separation from impurity gases (H<sub>2</sub>, N<sub>2</sub>, H<sub>2</sub>O, CO, Cl<sub>2</sub>, and CH<sub>4</sub>) via bilayer g-C<sub>3</sub>N<sub>4</sub> membrane. *Chin. Phys. B* **2019**, *28*, 8. [CrossRef]
24. Zhu, L.; Xue, Q.Z.; Li, X.F.; Wu, T.T.; Jin, Y.K.; Xing, W. C<sub>2</sub>N: An excellent two-dimensional monolayer membrane for He separation. *J. Mater. Chem. A* **2015**, *3*, 21351–21356. [CrossRef]
25. Wu, J.F.; Ding, S.Y.; Ye, S.H.; Lai, C. Grafting polymeric sulfur onto carbon nanotubes as highly-active cathode for lithium-sulfur batteries. *J. Energy Chem.* **2020**, *42*, 27–33. [CrossRef]
26. Park, J.H.; Lee, H.J.; Cho, J.Y.; Jeong, S.; Kim, H.Y.; Kim, J.H.; Seo, S.H.; Jeong, H.J.; Jeong, S.Y.; Lee, G.W.; et al. Highly Exfoliated and Functionalized Single-Walled Carbon Nanotubes as Fast-Charging, High-Capacity Cathodes for Rechargeable Lithium-Ion Batteries. *ACS Appl. Mater. Interfaces* **2020**, *12*, 1322–1329. [CrossRef] [PubMed]
27. Demir, S.; Fellah, M.F. A DFT study on Pt doped (4,0) SWCNT: CO adsorption and sensing. *Appl. Surf. Sci.* **2020**, *504*, 9. [CrossRef]
28. Zeb, S.; Peng, X.J.; Yuan, G.Z.; Zhao, X.X.; Qin, C.Y.; Sun, G.X.; Nie, Y.; Cui, Y.; Jiang, X.C. Controllable synthesis of ultrathin WO<sub>3</sub> nanotubes and nanowires with excellent gas sensing performance. *Sens. Actuator B-Chem.* **2020**, *305*, 12. [CrossRef]
29. Park, K.R.; Cho, H.B.; Lee, J.; Song, Y.; Kim, W.B.; Choa, Y.H. Design of highly porous SnO<sub>2</sub>-CuO nanotubes for enhancing H<sub>2</sub>S gas sensor performance. *Sens. Actuator B-Chem.* **2020**, *302*, 7. [CrossRef]
30. Hsu, J.H.; Yu, C. Sorting-free utilization of semiconducting carbon nanotubes for large thermoelectric responses. *Nano Energy* **2020**, *67*, 9. [CrossRef]
31. Guo, X.; Zhang, P.; Xue, J.M. Ti<sub>2</sub>CO<sub>2</sub> Nanotubes with Negative Strain Energies and Tunable Band Gaps Predicted from First-Principles Calculations. *J. Phys. Chem. Lett.* **2016**, *7*, 5280–5284. [CrossRef]
32. Jalil, A.; Agathopoulos, S.; Khan, N.Z.; Khan, S.A.; Kiani, M.; Khan, K.; Zhu, L. New physical insight in structural and electronic properties of InSb nano-sheet being rolled up into single-wall nanotubes. *Appl. Surf. Sci.* **2019**, *487*, 550–557. [CrossRef]
33. Abbasi, A.; Sardroodi, J.J.; Ebrahimzadeh, A.R.; Yaghoobi, M. Theoretical study of the structural and electronic properties of novel stanene-based buckled nanotubes and their adsorption behaviors. *Appl. Surf. Sci.* **2018**, *435*, 733–742. [CrossRef]
34. Abbasi, A.; Sardroodi, J.J. Interaction of sulfur trioxide molecules with armchair and zigzag stanene-based nanotubes: Electronic properties exploration by DFT calculations. *Adsorpt. J. Int. Adsorpt. Soc.* **2018**, *24*, 443–458. [CrossRef]
35. Eslami, M.; Moradi, M.; Moradi, R. DFT investigation of hydrogen adsorption on the C<sub>3</sub>N nanotube. *Vacuum* **2016**, *133*, 7–12. [CrossRef]
36. Tan, G.J.; Ohta, M.; Kanatzidis, M.G. Thermoelectric power generation: From new materials to devices. *Philos. Trans. R. Soc. A-Math. Phys. Eng. Sci.* **2019**, *377*, 20180450. [CrossRef]
37. Balandin, A.A. Thermal properties of graphene and nanostructured carbon materials. *Nat. Mater.* **2011**, *10*, 569–581. [CrossRef]
38. Zhu, T.J.; Liu, Y.T.; Fu, C.G.; Heremans, J.P.; Snyder, J.G.; Zhao, X.B. Compromise and Synergy in High-Efficiency Thermoelectric Materials. *Adv. Mater.* **2017**, *29*, 1605884. [CrossRef]
39. Sun, Y.; Di, C.A.; Xu, W.; Zhu, D.B. Advances in n-Type Organic Thermoelectric Materials and Devices. *Adv. Electron. Mater.* **2019**, *5*, 1800825. [CrossRef]
40. Perumal, S.; Roychowdhury, S.; Biswas, K. Reduction of thermal conductivity through nanostructuring enhances the thermoelectric figure of merit in Ge<sub>1-x</sub>BixTe. *Inorg. Chem. Front.* **2016**, *3*, 125–132. [CrossRef]
41. Jood, P.; Ohta, M.; Kunii, M.; Hu, X.K.; Nishiate, H.; Yamamoto, A.; Kanatzidis, M.G. Enhanced average thermoelectric figure of merit of n-type PbTe<sub>1-x</sub>Ix-MgTe. *J. Mater. Chem. C* **2015**, *3*, 10401–10408. [CrossRef]
42. Xu, Y.; Li, Z.Y.; Duan, W.H. Thermal and Thermoelectric Properties of Graphene. *Small* **2014**, *10*, 2182–2199. [CrossRef] [PubMed]
43. Avery, A.D.; Zhou, B.H.; Lee, J.; Lee, E.S.; Miller, E.M.; Ihly, R.; Wesenberg, D.; Mistry, K.S.; Guillot, S.L.; Zink, B.L.; et al. Tailored semiconducting carbon nanotube networks with enhanced thermoelectric properties. *Nat. Energy* **2016**, *1*, 16033. [CrossRef]
44. Brownlie, L.; Shapter, J. Advances in carbon nanotube n-type doping: Methods, analysis and applications. *Carbon* **2018**, *126*, 257–270. [CrossRef]
45. Elapolu, M.S.R.; Tabarraei, A.; Reihani, A.; Ramazani, A. Phononic thermal transport properties of C<sub>3</sub>N nanotubes. *Nanotechnology* **2020**, *31*, 035705. [CrossRef]
46. Zhang, T.; Zhu, L. Giant reduction of thermal conductivity in a two-dimensional nitrogenated holey C<sub>2</sub>N nanosheet. *Phys. Chem. Chem. Phys.* **2017**, *19*, 1757–1761. [CrossRef] [PubMed]
47. De Volder, M.F.L.; Tawfick, S.H.; Baughman, R.H.; Hart, A.J. Carbon Nanotubes: Present and Future Commercial Applications. *Science* **2013**, *339*, 535–539. [CrossRef]
48. Gopejenko, V.; Gopejenko, A. Using Applications and Tools to Visualize ab initio Calculations Performed in VASP. In *Augmented Reality, Virtual Reality, and Computer Graphics, Aor 2018, Pt I*; DePaolis, L.T., Bourdot, P., Eds.; Springer: Cham, Switzerland, 2018; Volume 10850, pp. 489–496.
49. Hacene, M.; Anciaux-Sedrakian, A.; Rozanska, X.; Klahr, D.; Guignon, T.; Fleurat-Lessard, P. Accelerating VASP electronic structure calculations using graphic processing units. *J. Comput. Chem.* **2012**, *33*, 2581–2589. [CrossRef] [PubMed]
50. Hongzhiwei, Technology, Device Studio, Version 2021A, China. 2021. Available online: <http://iresearch.net.cn/cloudSoftware> (accessed on 1 March 2023).
51. Korth, M.; Thiel, W. Benchmarking Semiempirical Methods for Thermochemistry, Kinetics, and Noncovalent Interactions: OMx Methods Are Almost As Accurate and Robust As DFT-GGA Methods for Organic Molecules. *J. Chem. Theory Comput.* **2011**, *7*, 2929–2936. [CrossRef]

52. Togo, A.; Oba, F.; Tanaka, I. First-principles calculations of the ferroelastic transition between rutile-type and  $\text{CaCl}_2$ -type  $\text{SiO}_2$  at high pressures. *Phys. Rev. B* **2008**, *78*, 134106. [[CrossRef](#)]
53. Shuichi, N. Constant Temperature Molecular Dynamics Methods. *Prog. Theor. Phys.* **1991**, *103*, 1–46.
54. Jiang, J.W.; Wang, J.S.; Li, B.W. A nonequilibrium Green's function study of thermoelectric properties in single-walled carbon nanotubes. *J. Appl. Phys.* **2011**, *109*, 014326. [[CrossRef](#)]
55. Giannozzi, P.; Barone, O.; Bonfanti, P.; Bruneau, D.; Car, R.; Carnimeo, I.; Cavazzoni, C.; de Gironcoli, S.; Delugas, P.; Ruffino, F.F.; et al. Quantum ESPRESSO toward the exascale. *J. Chem. Phys.* **2020**, *152*, 154105. [[CrossRef](#)] [[PubMed](#)]
56. Majidi, R.; Odelius, M.; AlTaha, S. Structural and electronic properties of nitrogenated holey nanotubes: A density functional theory study. *Diam. Relat. Mat.* **2018**, *82*, 96–101. [[CrossRef](#)]
57. Alam, H.; Ramakrishna, S. A review on the enhancement of figure of merit from bulk to nano-thermoelectric materials. *Nano Energy* **2013**, *2*, 190–212. [[CrossRef](#)]

**Disclaimer/Publisher's Note:** The statements, opinions and data contained in all publications are solely those of the individual author(s) and contributor(s) and not of MDPI and/or the editor(s). MDPI and/or the editor(s) disclaim responsibility for any injury to people or property resulting from any ideas, methods, instructions or products referred to in the content.